Journal of Magnetic Resonance 205 (2010) 148–160

Contents lists available at ScienceDirect

Journal of Magnetic Resonance

journal homepage: www.elsevier.com/locate/jmr

Improved determination of FID signal parameters in low-field NMR

Juhani Dabek [a,*], Jaakko O. Nieminen [a], Panu T. Vesanen [a], Raimo Sepponen [b], Risto J. Ilmoniemi [a]

[a] Aalto University, Department of Biomedical Engineering and Computational Science, P.O. Box 12200, FI-00076 Aalto, Finland
[b] Aalto University, Department of Electronics, Finland

ARTICLE INFO

Article history:
Received 19 August 2009
Revised 15 April 2010
Available online 27 April 2010

Keywords:
NMR
Low-field NMR
FID
Fourier transform
Power spectrum
Lorentz peak
Exponential fit
Transverse relaxation time

ABSTRACT

In this work, novel methods are suggested for assessing signal parameters of the free induction decay (FID) in nuclear magnetic resonance (NMR) experiments. The FID signal was recorded in a microtesla field and analysed to determine its relaxation time, amplitude, Larmor frequency and phase. The challenge was posed by the narrow line width, whose related effects were investigated through simulations, also.

The developed methods give a new view on FID signal estimation in microtesla as well as lower and higher fields. It is shown that the transverse relaxation time of a sample can be accurately determined in the frequency domain by other means than the Lorentz peak half width. Also, with some realistic approximations, a simple functional form for the power spectrum Lorentz peak shape is proposed. As shown in this work, the inspection of the power spectrum instead of the absorption and dispersion Lorentzians is advantageous in the sense that the waveform is independent of the FID phase.

The automatic and efficient methods presented in this work incorporate an integral exponential fit, the fit of the power spectrum Lorentz peak and two ways to determine the FID phase. When there are sufficiently many data points in the Lorentz peak, the power spectrum Lorentz peak shape fit provides a quick, simple and accurate way of determining the amplitude, relaxation time and Larmor frequency of the FID. In the measurements of this work, however, the narrow line width led to establishing a more applicable method which is based on the exponential decay of the Lorentz peak with a temporally moving power spectrum window.

1. Introduction

In traditional nuclear magnetic resonance (NMR) experiments, the rapidly oscillating FID signals enable conventional estimation of the free induction decay (FID) parameters. When moving from the high-field (megahertz) regime down to the low-field (kilohertz or even below) regime, the sparse frequency spectra pose new challenges. Due to the experimental set-up relating to a pulse sequence with a single $\pi/2$ excitation, the determination of the inhomogeneous transverse relaxation time T_2^* was pursued. By applying a spin-echo type sequence, the pure transverse relaxation time T_2 could have been revealed, instead.

In high fields, T_2^* can be determined from the full width at half maximum (FWHM) of the FID peak at the *Larmor frequency* [1–3]. It may also be possible to evaluate T_2^* by fitting an exponentially attenuated sinusoid in the time-domain signal. Furthermore, in the time domain, more sophisticated methods such as building the signal vector into a matrix with the singular value decomposition (SVD) [5], the SVD–Lanczos algorithm [6–8], another kind of matrix manipulation [9], the minimum variance method to suppress noise [10], prior knowledge of signal poles [11], linear prediction [12], PowerSlicing making use of the FID exponential decay [13], or iteratively multiplying the time-domain signal with an exponential factor while observing the *Lorentz peak* height [4], can be used. Some general surveys of time-domain methods can be found in [14–16]. In the present study, using the FWHM to determine T_2^* was difficult because the narrow line width limited the number of data points near the peak. The time-domain analysis was also difficult because of the noise; the FID was not at all discernible to the naked eye.

The signal amplitude A could also have been determined in the time domain if the noise had been less dominating. In the frequency domain, again, the few data points in the Lorentz peak made it challenging to determine A. Very few points in the Lorentz peak made it also hard to determine the Larmor frequency f_L exactly. The phase φ of the FID signal was also unknown. Some existing methods, presented in e.g. [17,18], give a practical approach for determining φ, usually in order to correct the baseline of the absorption spectrum over a large bandwidth. In [19], one point from both the absorption and dispersion spectrum is used to this end. Reference [20] presents several methods for determining φ, some of which resemble the combined absorption and dispersion spectrum method in the present study, yet being different. Therein, and in [21], the phase-independent power spectrum is utilized to determine A, f_L and T_2^*. The latter reference makes use of the

* Corresponding author. Fax: +358 9 470 23182.
E-mail address: juhani.dabek@tkk.fi (J. Dabek).

1090-7807/$ - see front matter © 2010 Elsevier Inc. All rights reserved.
doi:10.1016/j.jmr.2010.04.013

least-squares (LS) method in Lorentz peak shape fitting, which most closely resembles the method in the present study.

In this work, novel approaches for determining T_2^*, A, φ and f_L of the FID signal are proposed in order to solve the challenges associated with a low-frequency FID. It should be noted that the methods are applicable with precision in high-field NMR as well. The determination of the FID parameters involves four different views on the FID signal: the full-length Fourier transform (FT) power spectrum (PS); a sequence of short-term PSs with an exponential decay of the Lorentz peak height; the real and imaginary parts of the full-length FT; and the temporal FID signal. Temporal inspection yields the phase of the FID signal.

The four views on the FID signal benefit from some new mathematical approaches. These include the fitting of an exponential function and the fitting of the PS Lorentz peak shape by taking the noise into account in an efficient way. These procedures enable the determination of T_2^*, A and f_L. The one remaining parameter describing the FID, φ, can be estimated from the absorption and dispersion Lorentzians (the real and imaginary parts of the FID FT, respectively). Another approach of simply correlating a modelled FID with the measured signal in the time domain is also considered. These fitting methods were investigated also through simulations.

For exponential fitting, a new method based on integration of the equation of an exponential signal is proposed. Several methods for exponential fitting are known [22–24]. One of the most similar ones, presented in [25], also utilises integrating the exponential equation. However, the method developed here makes use of all the relevant first integrals and takes into account the noise in the data in an efficient way. It also works for non-uniformly spaced data.

In the literature, e.g. [1,3], the FID signal, in the frequency domain, is most often characterised by the absorption and dispersion Lorentzians, whose analytical forms are well-known. In this context, several methods for determining T_2^*, A and f_L are known. The spectral representation allows inspection of narrow frequency bands, which contributes to the increased speed of the fitting algorithms. The spectral methods make use of, e.g., the area under the Lorentz peak, SVD-based approaches and other ones similar to the time-domain approaches. Also, iterative curve fitting methods have been proposed, making use of the Lorentzian, Gaussian or Voigt lineshapes [26]. In this work, the PS Lorentzian is handled, and its analytical form before and after approximations are derived.

The presented methods can be applied at all NMR field strengths, and, especially at low fields. For example, measurements in the Earth's field with $B \approx 50$ μT [27,28] are often compromised by the temporal fluctuation of B. Thus, signal averaging is challenging, and could benefit from enhanced determination of T_2^*, A, φ and f_L from fewer averages, or, even the raw FID signal. In the following, the methods for determining the parameters are presented.

2. Methods

For determining the FID parameters, properties of the finite-length FT need to be studied, as well as the fitting of an exponential function. To determine φ, also correlation is handled. However, first the measurements are reviewed.

2.1. Measurement facilities

The NMR measurements were performed at the BioMag Laboratory at Helsinki University Central Hospital. Superconducting quantum interference devices (SQUIDs) submerged in liquid helium inside a Dewar vessel were used as detectors. The apparatus containing the SQUIDs, manufactured by Elekta Ltd., was designed for magnetocardiography (MCG) measurements [29] but was also suited for NMR measurements in low fields with an addition of magnetic fields for polarisation and measurement. In order to reduce external magnetic field noise, the measurements were performed inside a magnetically shielded room (MSR). The SQUID detector array included 33 magnetometers and 66 planar gradiometers, which measure magnetic fields and their gradients, respectively. For a good discussion on low-field measurements with SQUIDs in comparison to measurements utilising Faraday induction, see [30].

A 10-ml tap water sample was polarised inside the MSR with a quadrupolar permanent magnet set-up. The quadrupole consisted of two attached and rectilinear pairs of permanent magnets opposing each other with a spacing of approximately 2 cm. The permanent magnets were cylinders of radius 1 cm and height 1 cm. The magnetic field over the sample at a distance of approximately 1–3 cm from the quadrupole varied between approximately 30 and 200 mT. The quadrupolar set-up was used to minimise the unwanted field at the walls of the MSR.

After the polarisation, the sample was transferred to beneath the SQUIDs. Then, a measurement field $B \approx 2$ μT, produced by a 1.3-m long solenoid with 400 turns per metre, was turned on. The transfer of the sample and switching on the measurement field took approximately 2 s. The measurement field caused the sample's magnetic moment precession (FID). The symmetry axes of the permanent magnet quadrupole and the measurement field electromagnet were orthogonal to each other.

The recorded signals were real, since no quadrature detection was applied. The sampling frequency was 1000 Hz, and the recorded signals were band-pass filtered in the hardware from DC components to about 300 Hz. The removal of DC components had a distinct effect on the signals; if a rectangular pulse train is measured, the edges reproduce in the recorded signal but the plateaus diminish exponentially towards zero. In the following Subsections, the mathematical apparatus needed for the determination of A, T_2^*, f_L and φ is presented.

2.2. Analysis of the properties of the Lorentz peak

The basis of NMR is the FID signal recorded from a sample containing, e.g., hydrogen nuclei (protons), as in this work. The temporal signal can be represented by

$$s_L(t) = \begin{cases} 0, & \text{when } t < 0 \\ Ae^{-t/T_2^*}\cos(\omega_L t + \varphi) & \text{when } t \geqslant 0 \end{cases}, \tag{1}$$

where $\omega_L = 2\pi f_L = 2\pi\gamma B$ is the angular Larmor frequency with the gyromagnetic ratio for hydrogen $\gamma = 42.58$ Hz/μT and B the magnetic field. The frequency spectrum $\mathscr{F}$ of this signal is obtained through a finite-length discrete FT as

$$\mathscr{F}\{s_L(n\Delta t)\}(\omega) = \frac{1}{\sqrt{\mathscr{N}(s_L, n_0, N, \Delta t)}} \sum_{n=n_0}^{n_0+N-1} s_L(n\Delta t)e^{-i\omega n\Delta t}, \tag{2}$$

where ω is the angular frequency, N the number of samples, Δt the time step, $n_0\Delta t = t_0 \geqslant 0$ the starting time instant and $\mathscr{N}(s_L, n_0, N, \Delta t) = N/\Delta t$ is a normalisation factor, derived in Appendix A.

2.2.1. The temporal exponential decay of the FID Fourier transform

In the following, the exponential decay of the FID FT in a temporally progressing window is first derived. Thereafter, the contribution of noise is also taken into account. These allow, especially, determining an estimate for the relaxation time, $\widehat{T}_2^*$.

Inserting $s_L(n\Delta t)$ from Eq. (1) to Eq. (2),

$$S_L(\omega, n_0\Delta t, N\Delta t) = \sqrt{\Delta t/N}\sum_{n=n_0}^{n_0+N-1} Ae^{-n\Delta t/T_2^*}\cos(\omega_L n\Delta t + \varphi)e^{-i\omega n\Delta t} \tag{3}$$

$$= \sqrt{\Delta t/N}\cdot Ae^{-t_0/T_2^*}\sum_{n=0}^{N-1} e^{-n\Delta t/T_2^*} \cdot\cos(\omega_L[n\Delta t + t_0] + \varphi)e^{-i\omega(n\Delta t + t_0)}, \tag{4}$$

where the second equality holds after the substitution $(n\Delta t + t_0) \rightarrow n\Delta t$. Furthermore, when $2\pi f_L = \omega_L \gg 1/T_2^*$, the last expression may be approximated by

$$S_L(\omega, t_0, N\Delta t) \approx \sqrt{\Delta t/N} \cdot A e^{-t_0/T_2^*} \sum_{n=0}^{N-1} e^{-n\Delta t/T_2^*} \cos(\omega_L n\Delta t + \varphi) e^{-i\omega n\Delta t}. \tag{5}$$

In the region of interest, i.e., at the Larmor frequency, this holds approximately since the phase shifts in $\cos(\cdot)$ and $e^{(\cdot)}$ remain the same, and T_2^* is much longer than an oscillatory cycle. In the present study, $f_L \approx 100$ Hz and $1/T_2^* \approx 1\ s^{-1}$ [31]. Finally, the FT can be written as

$$S_L(\omega, t_0, N\Delta t) \approx e^{-t_0/T_2^*} S_L(\omega, 0, N\Delta t). \tag{6}$$

In the frequency domain, the Lorentz peak is located at f_L. Eq. (6) shows that it will decay according to T_2^* as the time window of the FT is shifted forward in time.

From now on, the PS is investigated, which gives directly a means to evaluate the standard deviation of noise at f_L. Another major advantage with the PS Lorentz peak, as opposed to the absorption (or dispersion) Lorentz peak, is that its form is independent of the yet unknown φ. Thus, from Eq. (6),

$$|S_L(\omega, t_0, N\Delta t)|^2 \approx e^{-2t_0/T_2^*} |S_L(\omega, 0, N\Delta t)|^2. \tag{7}$$

The measured signal is assumed to be the sum of the FID and noise $\eta(t)$ that is white around the Larmor frequency, i.e.,

$$u_L(t) = s_L(t) + \eta(t). \tag{8}$$

The contribution of $\eta(t)$ on the PS is analysed in Appendix B.

Combining Eqs. (7) and (B.6) gives a convenient equation for the exponential decay of the PS Lorentz peak height as

$$|U_L(\omega, t_0, N\Delta t)|^2 \approx |S_L(\omega, 0, N\Delta t)|^2 e^{-2t_0/T_2^*} + \sigma_\eta^2. \tag{9}$$

When the PS of the signal is calculated over a sequence of time windows and evaluated at the Larmor frequency, T_2^* can be determined from Eq. (9). From the same fit, $|S_L(\omega_L,0,N\Delta t)|^2$ and σ_η are also obtained.

The Larmor frequency can be determined from the location of the Lorentz peak in the PS of the entire FID signal. If the recorded signal duration $N\Delta t \gg T_2^*$, a good estimate $\hat{\omega}_L$ for the Larmor frequency is obtained. Also, according to the Nyquist sampling theorem, $f_L \leqslant 1/(2\Delta t)$ has to hold to avoid aliasing.

2.2.2. Estimating the signal amplitude

After the estimates $\hat{\omega}_L, \widehat{T}_2^*$ and $\hat{\sigma}_\eta$ have been determined, A can be estimated numerically by making use of the noiseless FID signal PS, as in Appendix C.1. For this purpose, it is best to use the full-length FID signal with N_{tot} samples. Starting from the relation

$$|U_L(\omega_L, 0, N_{tot}\Delta t)|^2 \approx |S_L(\omega_L, 0, N_{tot}\Delta t)|^2 + \sigma_\eta^2, \tag{10}$$

and using Eq. (C.18), the amplitude A is

$$A(\hat{\omega}_L, \omega_L) \approx \frac{2\sqrt{|U_L(\omega_L, 0, N_{tot}\Delta t)|^2 - \sigma_\eta^2}}{\sqrt{\frac{\Delta t}{N_{tot}}} \sqrt{\frac{1 + e^{-2N_{tot}\Delta t/T_2^*} - 2e^{-N_{tot}\Delta t/T_2^*} \cos([\hat{\omega}_L - \omega_L]N_{tot}\Delta t)}{1 + e^{-2\Delta t/T_2^*} - 2e^{-\Delta t/T_2^*} \cos([\hat{\omega}_L - \omega_L]\Delta t)}}}, \tag{11}$$

where ω_L is the true, unknown, Larmor frequency. The angular frequency resolution of the FT is $2\pi/(N_{tot}\Delta t)$. Thus, the maximum error in the Lorentz peak position is half of this: $\Delta\omega_L = \pi/(N_{tot}\Delta t)$. Therefore, assuming that the Lorentz peak is approximately symmetric, an upper bound for the original signal amplitude can be obtained by computing $A(\hat{\omega}_L + \Delta\omega_L, \hat{\omega}_L)$. The lower bound is simply $A(\hat{\omega}_L, \hat{\omega}_L)$.

2.3. Fitting of an exponential function

Next, the non-iterative method for exponential LS fitting is derived. It is based on integrating the exponential function; differentiating the function to obtain a LS fit was also attempted, but proved unstable. In contrast, the integration method is very stable.

The measurements are assumed to yield two coordinates (x,y) per data point that are distributed as

$$y(x) = ae^{bx} + c. \tag{12}$$

The constants a, b and c are to be determined from the measurements.

Eq. (12) is first integrated from x_m to x_n:

$$Y(x_n) - Y(x_m) = \frac{a}{b}(e^{bx_n} - e^{bx_m}) + c(x_n - x_m). \tag{13}$$

Substituting for the exponential terms from Eqs. (12) to (13) yields

$$Y(x_n) - Y(x_m) = \frac{1}{b}[y(x_n) - y(x_m)] + c(x_n - x_m). \tag{14}$$

From now on, all integrals satisfying $x_n > x_m$ will be considered. Let $\mathbf{x}$, $\mathbf{y}$ and $\mathbf{Y}$ denote vectors with elements $x_{n_k} - x_{m_k}, y(x_{n_k}) - y(x_{m_k})$ and $Y(x_{n_k}) - Y(x_{m_k})$, respectively; m_k and n_k denote the indices m and n for the kth element. The number of elements in the vectors is $M = P(P-1)/2$, where P is the original number of data points. Thus, Eq. (14) can be written as

$$\mathbf{Y} = \frac{1}{b}\mathbf{y} + c\mathbf{x}. \tag{15}$$

The LS solution for the constants in this equation is

$$\begin{bmatrix} 1/\hat{b} \\ \hat{c} \end{bmatrix} = ([\mathbf{y}\ \mathbf{x}]^T[\mathbf{y}\ \mathbf{x}])^{-1}[\mathbf{y}\ \mathbf{x}]^T\mathbf{Y}. \tag{16}$$

From Eq. (16), estimates for b and c can be solved:

$$\hat{b} = \frac{|\mathbf{x}|^2|\mathbf{y}|^2 - (\mathbf{x}^T\mathbf{y})^2}{|\mathbf{x}|^2(\mathbf{y}^T\mathbf{Y}) - (\mathbf{x}^T\mathbf{y})(\mathbf{x}^T\mathbf{Y})} \quad \text{and} \tag{17}$$

$$\hat{c} = \frac{|\mathbf{y}|^2(\mathbf{x}^T\mathbf{Y}) - (\mathbf{x}^T\mathbf{y})(\mathbf{y}^T\mathbf{Y})}{|\mathbf{x}|^2|\mathbf{y}|^2 - (\mathbf{x}^T\mathbf{y})^2}. \tag{18}$$

It will be assumed that around the Larmor frequency, x and y have additive white noise μ and v, respectively; the noiseless variables are denoted by subscript 0. Thus, the elements of the vectors $\mathbf{x}$, $\mathbf{y}$ and $\mathbf{Y}$ are

$$[\mathbf{x}]_k = (x_{0,n_k} + \mu_{n_k}) - (x_{0,m_k} + \mu_{m_k}), \tag{19}$$

$$[\mathbf{y}]_k = (y_{0,n_k} + v_{n_k}) - (y_{0,m_k} + v_{m_k}) \quad \text{and} \tag{20}$$

$$[\mathbf{Y}]_k = \sum_{n=m_k}^{n_k-1} (x_{n+1} - x_n)\frac{y_n + y_{n+1}}{2}, \tag{21}$$

whereafter $[\mathbf{x}_0]_k = x_{0,n_k} - x_{0,m_k}, [\mathbf{y}_0]_k = y_{0,n_k} - y_{0,m_k}, [\boldsymbol{\mu}]_k = \mu_{n_k} - \mu_{m_k}$ and $[\boldsymbol{v}]_k = v_{n_k} - v_{m_k}$ are assigned to yield

$$\mathbf{x} = \mathbf{x}_0 + \boldsymbol{\mu} \quad \text{and} \tag{22}$$

$$\mathbf{y} = \mathbf{y}_0 + \boldsymbol{v}. \tag{23}$$

The M sampled elements of μ and v are gathered in the vectors $\boldsymbol{\mu}$ and $\boldsymbol{v}$, respectively. The standard deviations of the noise variables are σ_μ and σ_v, respectively. The noise of the vector products in the solutions of $\hat{b}$ and $\hat{c}$ can be taken into account, as in Appendix D. The results are

$$|\mathbf{x}|^2 \approx |\mathbf{x}_0|^2 + 2M\sigma_\mu^2, \tag{24}$$

$$|\mathbf{y}|^2 \approx |\mathbf{y}_0|^2 + 2M\sigma_\nu^2, \tag{25}$$

$$\mathbf{x}^{\mathrm{T}}\mathbf{y} \approx \mathbf{x}_0^{\mathrm{T}}\mathbf{y}_0, \tag{26}$$

$$\mathbf{y}^{\mathrm{T}}\mathbf{Y} \approx \mathbf{y}_0^{\mathrm{T}}\mathbf{Y}_0 \quad \text{and} \tag{27}$$

$$\mathbf{x}^{\mathrm{T}}\mathbf{Y} \approx \mathbf{x}_0^{\mathrm{T}}\mathbf{Y}_0 + \sigma_\mu^2(\mathbf{y}^+)^{\mathrm{T}}\mathbf{1}, \tag{28}$$

where the elements of the vector $\mathbf{y}^+$ are sums of the y coordinates at the integration limits $\left(y_k^+ = y_{m_k} + y_{n_k}\right)$. The vector $\mathbf{1}$ is an M-dimensional vector of 1's.

Finally, the solutions in the integral method read

$$\hat{b} = \frac{\left[|\mathbf{x}|^2 - 2M\sigma_\mu^2\right]\left[|\mathbf{y}|^2 - 2M\sigma_\nu^2\right] - (\mathbf{x}^{\mathrm{T}}\mathbf{y})^2}{\left[|\mathbf{x}|^2 - 2M\sigma_\mu^2\right](\mathbf{y}^{\mathrm{T}}\mathbf{Y}) - (\mathbf{x}^{\mathrm{T}}\mathbf{y})\left[\mathbf{x}^{\mathrm{T}}\mathbf{Y} - \sigma_\mu^2(\mathbf{y}^+)^{\mathrm{T}}\mathbf{1}\right]} \tag{29}$$

and

$$\hat{c} = \frac{\left[|\mathbf{y}|^2 - 2M\sigma_\nu^2\right]\left[\mathbf{x}^{\mathrm{T}}\mathbf{Y} - \sigma_\mu^2((\mathbf{y}^+)^{\mathrm{T}}\mathbf{1})\right] - (\mathbf{x}^{\mathrm{T}}\mathbf{y})(\mathbf{y}^{\mathrm{T}}\mathbf{Y})}{\left[|\mathbf{x}|^2 - 2M\sigma_\mu^2\right]\left[|\mathbf{y}|^2 - 2M\sigma_\nu^2\right] - (\mathbf{x}^{\mathrm{T}}\mathbf{y})^2}. \tag{30}$$

The one remaining constant $\hat{a}$ will be solved from Eq. (12). Note that in the following, the vectors contain only P elements, and they can be distinguished from the vectors above by the bar on top of them. A vector with elements $\exp(\hat{b}x_n)$ will be denoted by $\bar{\mathbf{e}}$, and the vectors $\bar{\mathbf{1}}$ and $\bar{\mathbf{y}}$ have elements 1 and y_n, respectively. Starting from

$$\bar{\mathbf{y}} = \hat{a}\bar{\mathbf{e}} + \hat{c}\bar{\mathbf{1}}, \tag{31}$$

and multiplying by the vector $\bar{\mathbf{1}}$, and solving for $\hat{a}$, one gets

$$\hat{a} = \frac{\bar{\mathbf{y}}^{\mathrm{T}}\bar{\mathbf{1}} - P\hat{c}}{\bar{\mathbf{e}}^{\mathrm{T}}\bar{\mathbf{1}}}. \tag{32}$$

The computational cost for evaluating $\hat{a}$ depends on the number of data points as $\mathcal{O}(P)$ due to the computed vector products. It is not necessary to consider noise in the vector products because the vectors are uncorrelated.

The strength of the integral fitting solution is that it uses all the pairwise relations between the data points. The computational cost of this method depends on the number of data points as $\mathcal{O}(P^2)$. This is due to the fact that there are $M = P^2/2 - P/2$ elements in the dot products of $\hat{b}$ and $\hat{c}$, and only P in $\hat{a}$.

The only parameters needed in the integral fitting are the data points' standard deviations in the x and y directions. In the special case that there is no noise in the x direction, an iterative method is proposed for determining the noise in the y direction, see Appendix E.

2.4. Power spectrum Lorentz peak shape fitting

The parameters of the FID signal can also be determined from the Lorentz peak. Let the starting point be the PS Lorentz peak, Eq. (C.15) in Appendix C with the mentioned approximations. Denoting $|y|^2 = |U_{\mathrm{L}}(\omega, t_0, N\Delta t)|^2$, Eq. (C.15) may be rewritten as

$$[2\omega_{\mathrm{L}}]\cdot\omega|y|^2 + \left[-(1/T_2^*)^2 - \omega_{\mathrm{L}}^2\right]\cdot|y|^2 + [A^2/4N\Delta t]\cdot 1 = \omega^2|y|^2. \tag{33}$$

Picking up Q samples from the PS, and denoting the nth ω and $|y|^2$ by ω_n and $|y_n|^2$, respectively, the equation can be discretised to

$$\underbrace{\begin{bmatrix} \omega_1|y_1|^2 & |y_1|^2 & 1 \\ \vdots & \vdots & \vdots \\ \omega_Q|y_Q|^2 & |y_Q|^2 & 1 \end{bmatrix}}_{\mathbf{Z}} \underbrace{\begin{bmatrix} 2\omega_{\mathrm{L}} \\ -(1/T_2^*)^2 - \omega_{\mathrm{L}}^2 \\ A^2/4N\Delta t \end{bmatrix}}_{\zeta} = \underbrace{\begin{bmatrix} \omega_1^2|y_1|^2 \\ \vdots \\ \omega_Q^2|y_Q|^2 \end{bmatrix}}_{\mathbf{z}}. \tag{34}$$

As indicated, this may be written as

$$\mathbf{Z}\zeta = \mathbf{z}. \tag{35}$$

The LS solution to this equation reads

$$\zeta = (\mathbf{Z}^{\mathrm{T}}\mathbf{Z})^{-1}\mathbf{Z}^{\mathrm{T}}\mathbf{z}. \tag{36}$$

In the following Subsection, the noise in the data is taken into account.

2.4.1. Noise considerations

The effect of noise has been studied in more detail in Appendix F, making use of the FID signal's noise η, that is assumed white around the Larmor frequency, with standard deviation σ_η. Using Eq. (F.7), the corrected power spectrum can be written as

$$|y_{01}|^2 \approx |y|^2 - \sigma_\eta^2. \tag{37}$$

The same kind of analysis is carried out for $|y|^4$. Using Eq. (F.10), where the corrected variable is marked with $|y_{02}|^4$, results in

$$|y_{02}|^4 \approx |y|^4 - 4\sigma_\eta^2|y|^2. \tag{38}$$

2.4.2. Taking the noise into account in the fit

Now, the noise in the matrix products of $\mathbf{Z}$ and $\mathbf{z}$ can be taken into account. Assuming the frequency parameter ω noiseless, one simply substitutes $|y_{01}|^2$ for $|y|^2$ and $|y_{02}|^4$ for $|y|^4$. The 3×3 matrix $\mathbf{Z}^{\mathrm{T}}\mathbf{Z}$ in Eq. (36) can be written as

$$\mathbf{Z}^{\mathrm{T}}\mathbf{Z} = \sum_{n=0}^{Q-1}\begin{bmatrix} \omega_n^2|y_{02n}|^4 & \omega_n|y_{02n}|^4 & \omega_n|y_{01n}|^2 \\ \omega_n|y_{02n}|^4 & |y_{02n}|^4 & |y_{01n}|^2 \\ \omega_n|y_{01n}|^2 & |y_{01n}|^2 & 1 \end{bmatrix}. \tag{39}$$

The matrix–vector product in the same equation can be written as

$$\mathbf{Z}^{\mathrm{T}}\mathbf{z} = \sum_{n=0}^{Q-1}\begin{bmatrix} \omega_n^3|y_{02n}|^4 \\ \omega_n^2|y_{02n}|^4 \\ \omega_n^2|y_{01n}|^2 \end{bmatrix}. \tag{40}$$

Now, ζ can be written out with these corrections:

$$\zeta = \left(\sum_{n=0}^{Q-1}\begin{bmatrix} \omega_n^2|y_{02n}|^4 & \omega_n|y_{02n}|^4 & \omega_n|y_{01n}|^2 \\ \omega_n|y_{02n}|^4 & |y_{02n}|^4 & |y_{01n}|^2 \\ \omega_n|y_{01n}|^2 & |y_{01n}|^2 & 1 \end{bmatrix}\right)^{-1}\left(\sum_{n=0}^{Q-1}\begin{bmatrix} \omega_n^3|y_{02n}|^4 \\ \omega_n^2|y_{02n}|^4 \\ \omega_n^2|y_{01n}|^2 \end{bmatrix}\right). \tag{41}$$

Finally, from ζ, defined in Eq. (34), the FID signal characteristic parameters may be solved:

$$f_{\mathrm{L}} = \frac{\omega_{\mathrm{L}}}{2\pi} = \frac{\zeta_1}{4\pi}, \tag{42}$$

$$T_2^* = \frac{1}{\sqrt{-\zeta_2 - \omega_{\mathrm{L}}^2}} = \frac{1}{\sqrt{-\zeta_2 - (\zeta_1/2)^2}} \quad \text{and} \tag{43}$$

$$A = 2\sqrt{N\Delta t\zeta_3}, \tag{44}$$

where the subscripted ζ's refer to the elements of ζ.

2.5. Determining the phase of the FID signal

It has been shown how f_{L}, T_2^* and A can be determined from the PS. For φ, other approaches are needed. First, the use of absorption and dispersion Lorentzians is proposed. Then, a correlation method is given.

2.5.1. The phase from the complex Lorentzian

In this Subsection, the complex Lorentzian comprising the absorption and dispersion Lorentzians is considered. The noise can be neglected since it is zero mean in the FT and the eventual equation for the determination of φ.

The starting point is Eq. (C.3), i.e., the FT of the FID signal in Eq. (1). It can be shown similarly as in Appendix C that the second term in the FT can be neglected when $\omega_L \gg 1/T_2^*$. The real amplitude coefficient may be discarded, also.

The Lorentz peak is considered over the frequency samples ω_m covering it. Close around the Lorentz peak, constructing a vector $\mathbf{y}$ with elements $S_L(\omega_m, 0, N\Delta t)$ and a vector $\mathbf{g}$ with elements

$$g_m = \frac{e^{-\left(1/T_2^* - i\omega_L + i\omega_m\right)N\Delta t} - 1}{e^{-\left(1/T_2^* - i\omega_L + i\omega_m\right)\Delta t} - 1}, \tag{45}$$

Eq. (C.3) can be written as

$$\mathbf{y} \approx \sqrt{\frac{\Delta t}{N}} \cdot \frac{A}{2} \cdot e^{i\varphi}\mathbf{g}. \tag{46}$$

This equation can be solved for φ by taking the inner product of the equation with a vector of ones, $\mathbf{1}$:

$$e^{i\varphi} \approx \frac{\mathbf{y}^T\mathbf{1}}{\sqrt{\frac{\Delta t}{N}} \cdot \frac{A}{2} \cdot \mathbf{g}^T\mathbf{1}}. \tag{47}$$

The phase is recovered by computing

$$\varphi \approx \arctan\left(\frac{\mathrm{Im}\left[(\mathbf{y}^T\mathbf{1})/(\mathbf{g}^T\mathbf{1})\right]}{\mathrm{Re}\left[(\mathbf{y}^T\mathbf{1})/(\mathbf{g}^T\mathbf{1})\right]}\right). \tag{48}$$

2.5.2. The phase by correlation

Another method to estimate φ is correlating a simulated FID $s_L(\tilde{\varphi}, n\Delta t) = Ae^{-n\Delta t/T_2^*}\cos(\omega_L n\Delta t + \tilde{\varphi}), t \geqslant 0$, with the noisy measured signal $u_L(\varphi, n\Delta t) = Ae^{-n\Delta t/T_2^*}\cos(\omega_L n\Delta t + \varphi) + \eta(n\Delta t), t \geqslant 0$, where the N samples are indexed by n with a time step Δt. As derived in Appendix G, the correlation has a proportionality relation

$$c\{s_L(\tilde{\varphi}, n\Delta t), u_L(\varphi, n\Delta t)\} \propto \cos(\tilde{\varphi} - \varphi). \tag{49}$$

The correlation maximum value is found by varying the test phase $\tilde{\varphi}$ over one full cycle, 2π. The corresponding argument $\tilde{\varphi}$ is the phase of the FID.

3. Results

In the following, the signal of a planar gradiometer was chosen for study. The aim was to determine the four FID parameters T_2^*, A, f_L and φ from the signal. First, the signal needed preprocessing.

3.1. Preprocessing

The steps of preprocessing are illustrated in Fig. 1, as well as the PS from the full signal. Accordingly, before the Fourier analysis, a slow exponential trend was subtracted from the signal. The fitting of a, b and c was performed with the method in Section 2.3. After this, the signal was low-pass filtered bidirectionally (Butterworth IIR, order 5) with a cutoff frequency of 2.5 Hz. The filtered signal was then subtracted from the signal. Thus the FID signal was preserved while taking unwanted low-frequency signal components away. The validity of high-pass filtering would have been more difficult to estimate visually.

It is to be noted that the constant term in the exponential fit (the term c in Eq. (12)) was revealed to be clearly different from 0. Thus, an exponential fit without a constant term would have performed poorly.

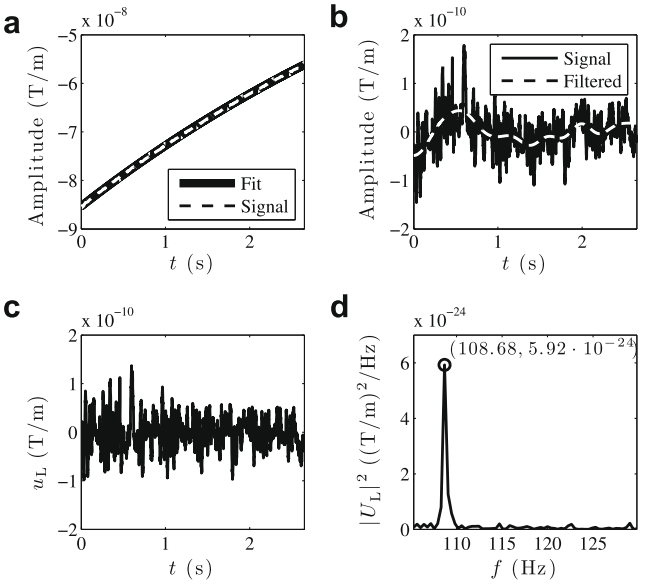

Fig. 1. Steps in the signal preprocessing: In (a), the original signal and an exponential fit are shown. In (b), the exponential trend has been subtracted from the signal. The low-pass filtered signal is also shown in (b). In (c), the difference of the two signals in (b), which is the final pre-processed signal, is shown. In (d), the final pre-processed signal has been Fourier-transformed to obtain the PS, $|U_L(2\pi f, 0, N_{tot}\Delta t)|^2$.

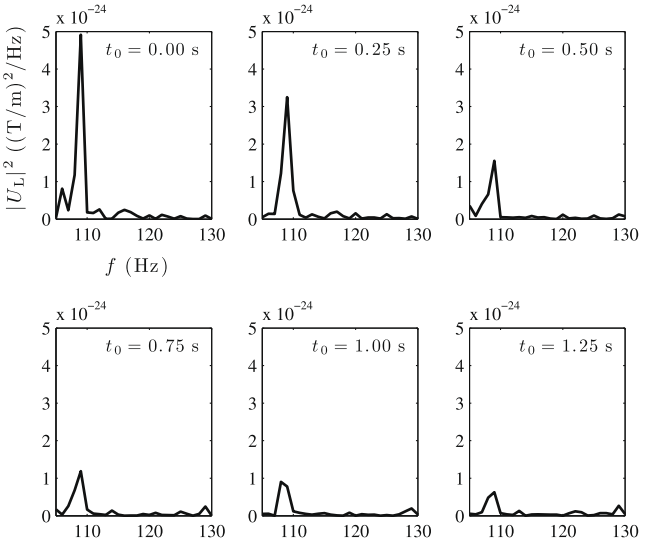

Fig. 2. FID PS peaks at times t_0 from the beginning of the a precession; the width of the time window is 1 s. The peak height decays exponentially according to $T_2^*/2$. The horizontal axes represent frequency f and the vertical axes spectral power $|U_L(2\pi f, t_0, N\Delta t)|^2$.

3.2. Fitting the FID parameters

Next, the sequence of FTs is considered for an exponential integral fit. Each Fourier window spans over a duration of 1 s. The first Fourier window PS is represented in Fig. 2 at $t_0 = 0.00$ s. The next window shown is the one with $t_0 = 0.25$ s and so forth until $t_0 = 1.25$ s. The last Lorentz peak is tiny compared to the first one because, according to Eq. (9), the peak's height decreases with time constant $T_2^*/2 \approx 0.5$ s.

In Fig. 3, the Lorentz peak heights, as in Fig. 2, are plotted against t_0. However, the window is moved with smaller steps, of length 10 ms. There are altogether $P = 166$ peaks forming equally many data points. The exponential fitting of parameters T_2^* and f_L by integration was performed by comparing Eqs. (9) and (12), and noting that

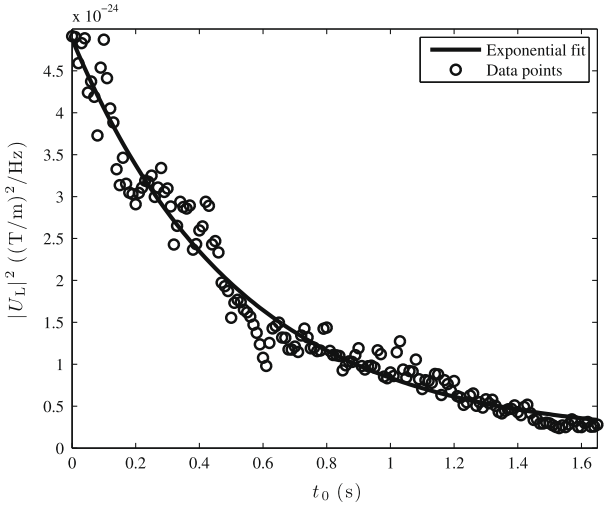

Fig. 3. Exponentially fitted FT FID peak heights. The time t_0 from the initial Fourier window is represented on the horizontal axis. The spectral power of the peak at Larmor frequency, $|U_L(\omega_L, t_0, N\Delta t)|^2$, is represented on the vertical axis.

Table 1
Fitting results by the integral method. See text for explanations.

Parameter (unit)	Value
$\hat{a}$ ((T/m)^2/Hz)	$4.75 \cdot 10^{-24}$
$\hat{b}$ (1/s)	-1.90
$\hat{c}$ ((T/m)^2/Hz)	$1.30 \cdot 10^{-25}$
Δx (ms)	10
σ_μ (ms)	0
σ_v ((T/m)^2/Hz)	$2.26 \cdot 10^{-25}$
Error ((T/m)^2/Hz)	$2.25 \cdot 10^{-25}$

$$x = t_0, \tag{50}$$
$$y = |U_L(\omega_L, t_0, N\Delta t)|^2, \tag{51}$$
$$a = |S_L(\omega_L, 0, N\Delta t)|^2, \tag{52}$$
$$b = -2/T_2^* \quad \text{and} \tag{53}$$
$$c = \sigma_\eta^2, \tag{54}$$

where $N = 1000$ is the number of data points in the sequential time windows. The selection of the moving FT window length is a trade-off between data points in the exponential fit and the frequency resolution. Having 166 data points in the fit and 1000 samples in the FTs seemed a reasonable choice; the simulations in Section 3.3 show that with such a choice, T_2^* could be accurately recovered.

In Table 1, the results using the integral method are presented. The shown error was calculated by subtracting the fitted function from the data points in the y direction and taking the standard deviation of this. The value of the standard deviation σ_v used for the optimal fit, and presented in Section 2.3, was almost the same. The standard deviation σ_μ, as presented in the same Section, was evaluated to be 0 because of the precise manner by which the Fourier window was translated over the time signal (10 ms at a time).

A comparison to the new integral-based fitting method was performed according to another integral-based method [22]. The target equation consisted of two exponential terms:

$$y = a_1 e^{-b_1 x} + a_2 e^{-b_2 x}. \tag{55}$$

In the present study, it was assumed *a priori* that $b_2 = 0$. Thus, Eq. (55) reduced to the form of Eq. (12). The fit was successful, but the error, calculated in the same way as above, was 31% higher than the one acquired with the new method. The main differences between this method and the present one are that it uses only $P - 1$ numerical integrals from the data, and it does not take the noise of the data into account.

Using the fit results of the new method, T_2^* and f_L of the water sample were estimated to be

$$\hat{T}_2^* = -2/\hat{b} \approx 1.05 \text{ s} \quad \text{and} \tag{56}$$
$$\hat{f}_L = \frac{\hat{\omega}_L}{2\pi} \approx (108.68 \pm 0.19) \text{ Hz}, \tag{57}$$

where $\hat{f}_L$ was observed from the data of Fig. 1d. Its maximum error estimate is half of the frequency step. The noise level from the full-length power spectrum in the range [113, 130] Hz was estimated to be $\hat{\sigma}_\eta \approx 0.23 \cdot 10^{-12}$ (T/m)/$\sqrt{\text{Hz}}$. According to Eq. (54), the standard deviation of noise at f_L can be computed to be $\hat{\sigma}_\eta \approx 0.36 \cdot 10^{-12}$ (T/m)/$\sqrt{\text{Hz}}$. There is a difference in the noise levels due to the different lengths of the FTs.

As to the noise at f_L, a comparison in the same units as A reveals a value of $\sqrt{\hat{c}/\Delta t} \approx 11.41 \cdot 10^{-12}$ T/m. The final step is computing A. Now, since the condition $N\Delta t/T_2^* \gg 1$ fails, the theoretical value for the Lorentz peak height, $(AT_2^*)^2/(4N\Delta t)$ (see Appendix C), cannot be used to determine A. Instead, Eq. (11) is used to obtain a lower and upper boundary for the signal amplitude: $\widehat{A} \in [8.11, 11.03] \cdot 10^{-12}$ T/m.

The phase of the measured FID signal was estimated by the methods in Section 2.5. The use of the absorption and dispersion Lorentzian waveforms led to the result 0.38 rad. By using the correlation method, a value of 0.77 rad was obtained for $\hat{\varphi}$. The key results of the estimates are presented in Table 2.

3.2.1. The Lorentz peak shape fitting

Also, an attempt was made to estimate the FID parameters by the method of Lorentz peak fitting derived in Section 2.4; it proved difficult. According to simulations, when the Lorentz peak is represented by almost only one point, the LS solution matrix may have too low a rank to be inverted properly. An obvious reason for the difficulty of applying the method of Section 2.4 is that the approximation assumption $N\Delta t/T_2^* \gg 1$ which is needed, only barely holds. However, the measured FID peak was represented by slightly

Table 2
Key results of fitting. In the row titled Exp. fit, T_2^* was determined by the Lorentz peak height's exponential decay in a moving time window, using the integral exponential method, Eqs. (17) and (53). The Larmor frequency f_L was determined on the same row by checking its position in the full-length PS. Also, on the same row, the range for A was estimated by using an approximation for the Lorentz peak height in the full-length PS, Eq. (11). The φ with the subscript wav refers to the phase obtained by the Lorentz waveforms, Eq. (48), and the φ with the subscript corr refers to the estimate obtained by correlation, Eq. (49). The last column's σ_η reflects the frequency domain noise standard deviation at or near f_L. The row L. fit and L. fit z.p. contain the fitting results of direct Lorentz peak shape fitting and the same with zero padding, respectively, see Eqs. (42)–(44) and Fig. (4). The numbers of samples in the FT PSs in the T_2^* and σ_η columns with the three different methods were 1000, 2650 and 10,600 from the first row to the last row, respectively. In the columns A and f_L, the PSs had 2650 samples on the first and second row, and 10,600 samples on the last row. The determinations of the phases included all 2650 recorded samples.

	A (10^{-12} T/m)	T_2^* (s)	f_L (Hz)	φ_{wav} (rad)	φ_{corr} (rad)	σ_η (10^{-12} (T/m)/$\sqrt{\text{Hz}}$)
Exp. fit	$\in$[8.11, 11.03]	1.05	108.68 ± 0.19	0.38	0.77	0.36
L. fit	7.28	1.35	108.77			0.23
L. fit z.p.	9.85	0.84	108.60			0.11

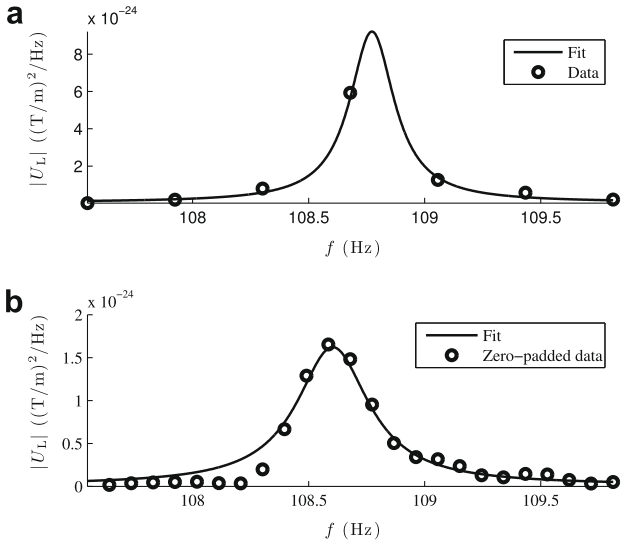

Fig. 4. Lorentz peak fitted by the application of the Lorentz peak shape. The peak in (a) has been computed directly from the FID, and the fit has been performed on the visible horizontal axis stretch. The peak in (b) has been computed by zero-padding the FID with three times as many zeros in the end as data points in the measured FID. The peak fit has been performed on an area 0.3 Hz to the left and right of the Lorentz peak top. The plotted fit has been extrapolated further away from that area. The vertical axis represents the PS $|U_L(2\pi f,\ 0,\ N_{tot}\Delta t)|^2$ in (a), and $|U_L(2\pi f,\ 0,\ 4N_{tot}\Delta t)|^2$ in (b) which is the PS of the zero-padded FID signal. The noise parameter for the fits was estimated in each case from the interval [113, 130] Hz.

more than one point, so the fitting was possible. The key results are presented in Table 2. The resulting fit is illustrated in Fig. 4.

3.3. Simulations

The fitting procedures of exponential decay, direct and zero-padded Lorentz peak shape, phase by Lorentz waveform and correlation were tested by simulations. The data are presented in Table 3.

The first simulation had $f_L = 108.68$ Hz, coinciding with a sampling point in the full-length PS. The second one had $f_L = 108.87$ Hz, appearing in the middle of two sampling points in the full-length PS, while agreeing on the other parameters of the first simulation. It can be seen that in both cases, the estimates for T_2^* are reproduced equally well with all methods, except for the zero-padding method. In the first simulation, all methods accurately agree on f_L, as could be expected. It is also logical that in the second simulation, f_L is half a frequency step off the correct one on the row titled Exp. fit, as the value is observed from the peak PS value's position on the frequency axis. The Lorentz peak shape fits agree precisely with the correct value. The estimated values of A are near the correct one, and the interval on the Exp. fit row behave as expected; in the first simulation, A appears approximately at the infimum of the interval and in the second simulation, it appears close to the supremum of the interval. As to the phase, both estimates are remarkably accurate when f_L coincides with a sampling point, whereas having it between them makes the phase estimates notably less accurate.

In the third simulation, the values of the second simulation were used, but noise from a measurement without an FID was superposed on the signal. The integral exponential fit estimate for T_2^* is still very accurate. The Lorentz peak shape fits give good estimates for f_L, and A is still close to the supremum obtained with Eq. (11).

In the fourth simulation, A was doubled, while the other parameters agreed with the third simulation. The parameter estimates have approximately the same level of accuracy as in the third simulation. In the following Sections, the implications of the simulations are discussed, along with other remarks.

4. Discussion

In this work, it was shown that getting the four characterising parameters of an FID can be achieved by using a moving window of FTs over the signal, the signal's full-length FT and the temporal signal. These are the inhomogeneous transverse relaxation time T_2^*, Larmor frequency f_L, amplitude A and phase φ.

The signal preprocessing featured an integral exponential fit and a bidirectional low-pass filtering. After this, the signal was sequentially short-term Fourier-transformed to obtain the exponential decay of the Lorentz peak in the PS. The height of the peak depends on T_2^* and A. In the preprocessing and the parameter estimation, the developed, integral-based and noise-corrected, exponential fitting method proved efficient and accurate. This method, and the Lorentz peak shape fitting, are briefly handled in the next Subsection, whereafter the fitting results pertaining to the FID are presented in the following Subsections.

4.1. Integral exponential fitting and the power spectrum Lorentz peak

A comparison between the new exponential fitting method and a previously reported method [22] was performed. The new method proved much more robust. This can be explained by two factors. First, the new method makes use of all relevant, numeri-

Table 3
Fitting results of four simulations with four consecutive rows per simulation. The rows titled Test represent values of parameters for constructing the simulation signals (see Table 2). The parameter σ_v is the time domain standard deviation of the measured noise that is assumed white around the Larmor frequency, superposed on the simulated FID.

	A (10^{-12} T/m)	T_2^* (s)	f_L (Hz)	φ_{wav} (rad)	φ_{corr} (rad)	σ_v (10^{-12} (T/m)/$\sqrt{\text{Hz}}$)
Test	9.50	1.05	108.68	1.00		0.00
Exp. fit	∈[9.49, 12.91]	1.05	108.68 ± 0.19	1.00	1.00	
L. fit	8.74	1.05	108.68			
L. fit z.p.	10.10	0.96	108.68			
Test	9.50	1.05	108.87	1.00		0.00
Exp. fit	∈[7.03, 9.56]	1.05	109.06 ± 0.19	0.89	0.45	
L. fit	10.26	1.05	108.87			
L. fit z.p.	10.10	0.96	108.87			
Test	9.50	1.05	108.87	1.00		8.66
Exp. fit	∈[7.25, 9.83]	1.04	108.68 ± 0.19	1.20	1.53	
L. fit	9.71	1.14	108.85			
L. fit z.p.	9.82	1.04	108.86			
Test	19.00	1.05	108.87	1.00		8.66
Exp. fit	∈[14.21, 19.29]	1.04	108.68 ± 0.19	1.15	1.55	
L. fit	20.18	1.11	108.85			
L. fit z.p.	19.80	1.01	108.87			

cally evaluated first integrals. Second, the method takes the noise in the data into account. The correct noise level can be estimated by the iterative method proposed in Appendix E.

The integral-based exponential fitting needs only two parameters which often can be estimated from the data prior to calculation: the noise in the x and y directions. Excluding the noise, the data are assumed to be uniformly distributed in the x direction.

Fitting of the PS Lorentz peak by using its formula proved difficult due to the peak consisting of very few points. However, the presented least squares solution for the fitting considers also noise in the signal and may prove useful for Lorentz peaks consisting of a better continuum of sample points in another application. Also, the Lorentz peak form fitting method takes into account the noise in the signal. The advantage of PS Lorentz peak over absorption or dispersion Lorentzians is that it is independent of φ.

4.2. Fitting results for T_2^* and A

With the exponential fit, the obtained value for the transverse (inhomogeneous) relaxation time, $T_2^* = 1.05$ s, is reasonable and in accordance with other studies: According to the results in [32], low-field measurements of distilled water yielded a value of pure $T_2 \approx 1.5$ s at 2.6 μT ($f_L \approx$ 110 Hz). According to another low-field NMR survey, a value of pure $T_2 \approx 1.3$ s was reported [33]. Thus, the results obtained in this work with a 10 ml tap water sample are of the correct order: the T_2^* is less than the pure T_2 for distilled water, as is to be expected. Thus, the main factors contributing to the decrease in T_2^* are probably the inhomogeneity of the measurement field and impurities in the tap water. They cause the nuclear spins to dephase, which reduces the relaxation time.

The direct Lorentz peak shape fitting result for T_2^* is 1.35 s; it is 0.84 s with zero-padding. When the Lorentz peak consists only of a few points, zero-padding of the time-domain signal adds more points to the peak. Thus, the peak shape fitting becomes easier. However, it seems that in this case the direct Lorentz peak shape fitting yields a more accurate result, because the zero-padding method adds data points to the peak incorrectly by visual inspection, see Fig. 4.

The estimates for T_2^* with the above-mentioned methods differ clearly from each other. The simulations can give a hint as to which one would be the most reliable estimate. It seems that the exponential fitting method is close to reality, while the direct Lorentz peak shape fitting gives an overestimate, and furthermore, padding zeros to the FID in the Lorentz peak shape fitting yields too low an estimate for T_2^*.

The range for the signal amplitude, $A \in [8.11, 11.03] \cdot 10^{-12}$ T/m, obtained by inspecting the Lorentz peak height, is realistic according to simulations. The result by using the direct Lorentz peak shape fitting is $A = 7.28 \cdot 10^{-12}$ T/m, and with zero-padding $A = 9.85 \cdot 10^{-12}$ T/m. These results fall on the edges of the aforementioned interval. The time-domain signal amplitude A is of the same magnitude as the time-domain noise at that frequency, $11.41 \cdot 10^{-12}$ T/m, obtained from the integral exponential fitting.

According to simulations, doubling the FID amplitude, while keeping the noise level the same, did not clearly affect the estimates of T_2^* and A. However, using a longer stretch of the FID signal improves the estimate accuracy due to more data points in the integral exponential fitting and the Lorentz peak. In this case, doubling the FID amplitude will also be helpful, thus decreasing the role of noise over the attenuated sinusoid.

According to the theory, doubling the FID signal amplitude increases the height of the Lorentz peak by a factor of 4, as can be seen analytically from Eq. (C.18). Assuming that the transverse relaxation, characterised by T_2^*, and the longitudinal relaxation, characterised by T_1, are of the same order of magnitude, an estimate for the signal increase by shifting the sample more quickly to the measurement position can be obtained. In the experiment, roughly doubling the signal amplitude could be achieved by shifting the sample from the permanent magnet to the SQUIDs $T_2^* \cdot \ln 2 \approx 0.7$ s faster, see Eq. (1). On the other hand, it always holds that $T_2^* < T_1$, so the signal increase could be slightly less.

4.3. Fitting results for f_L and φ

The Larmor frequency obtained from the measured FID by the direct Lorentz peak shape fitting method was 108.77 Hz; it was 108.60 Hz with zero-padding. The Larmor frequency, estimated by the location of the Lorentz peak in the FT, (108.68 ± 0.19) Hz, is in accordance with these results. The Larmor frequency estimates indicate the measurement field to have had the strength 2.55 μT. This is of the order estimated with the used coil geometry.

Eventually, φ was evaluated by two methods. The average φ was approximately 0.57 rad ≈ 33°. The variation of the two results, 0.40 rad ≈ 23°, indicates, once again, that with the narrow line width and relatively few data points, it is difficult to calculate precise parameters of the signal.

5. Conclusions

From a low-resolution FID signal, it was possible to determine the FID parameters. The studied FID was real-valued; however, the proposed methods easily extend to a complex FID signal. The methods are nearly automatic; very little manual intervention is necessary, mainly in the FID signal preprocessing. For the integral noise-corrected exponential fit, the acronym INC-ExpFit is suggested; for the power-spectral noise-corrected Lorentz peak fit, the name PoNC-LorFit is proposed. Both of these methods work with merely an assumption of noise that is white around the Larmor frequency, and that can be non-Gaussian. The whiteness of the noise should be a fair assumption, because the investigated frequency band around the Larmor frequency is rather narrow.

After the preprocessing, the presented methods perform quickly. In the case of narrow line width and very few data points in the Lorentz peak, the exponential decay of the PS Lorentz peak over sequential short-term FT PSs yields a reasonable estimate for T_2^*. In fact, according to simulations, this estimate for T_2^* is more accurate than the one with the Lorentz peak shape fitting. A crude estimate for f_L can be obtained from the full-length FT PS. An estimate interval for A can be computed by using a partial approximation for the height of the PS Lorentzian. It should also be noted that it is possible to determine the pure T_2 instead of T_2^* with the presented methods; the choise depends only on the NMR sequences used.

In case a low-noise and long signal acquisition can be carried out, the Lorentz peak most probably is represented by numerous data points, three of the FID parameters, T_2^*, f_L and A, can be quickly determined by fitting the form of the PS Lorentzian to the data. The phase φ can be determined separately by two methods: either from the FID FT or by correlating the modelled FID with the time-domain FID. In all of the methods presented in this work, the signal noise is taken into account, which improves the results. In the future, the methods may be extended to handle more than one exponentially attenuated sinusoid.

The presented methods are applicable at any NMR field strength and signal-to-noise ratio. In case it is desired to determine the four parameters underlying Lorentz peaks in a high-field PS, it is suggested that shorter data-acquisition times are possible when using the methods presented in this study. Thus, considerable speed-up of experiments could be expected. On the other hand, NMR in the Earth's magnetic field could be facilitated. Also, the NMR signal amplitude could be used to estimate the longitudinal relaxation time T_1 with an appropriate pulse sequence.

Acknowledgments

The authors wish to thank Dr. Juha Simola of Elekta Ltd. who helped in planning and executing the measurements, and Ms. Edith Grac who partly built the experimental set-up. The research leading to these results has received funding from the EU under the Grant agreement No. 200859. JD is also grateful to the Finnish Foundation for Technology Promotion for the personal grant.

Appendix A. Power spectrum normalisation

This Appendix pertains to Section 2.2. The PS normalisation factor $\mathcal{N}(h, n_0, N, \Delta t)$ can be determined for a time-domain signal $h(t)$ from

$$\sum_{m=0}^{N-1} |\mathcal{F}\{h(n\Delta t)\}(m\Delta\omega)|^2 = \sum_{n=n_0}^{n_0+N-1} |h(n\Delta t)|^2 \Delta t \tag{A.1}$$

$$\left(\approx \int_{t_0}^{t_0+N\Delta t} |h(t)|^2 dt\right) \tag{A.2}$$

$$\Rightarrow \frac{1}{\mathcal{N}(h, n_0, N, \Delta t)} \sum_{m=0}^{N-1} \left| \sum_{n=n_0}^{n_0+N-1} h(n\Delta t) e^{-im\Delta\omega n\Delta t} \right|^2 = \sum_{n=n_0}^{n_0+N-1} |h(n\Delta t)|^2 \Delta t \tag{A.3}$$

$$\Rightarrow \mathcal{N}(h, n_0, N, \Delta t) = \frac{\sum_{m=0}^{N-1} \left| \sum_{n=n_0}^{n_0+N-1} h(n\Delta t) e^{-im\Delta\omega n\Delta t} \right|^2}{\sum_{n=n_0}^{n_0+N-1} |h(n\Delta t)|^2} \cdot \frac{1}{\Delta t} = \frac{N}{\Delta t}, \tag{A.4}$$

where N is the number of samples, Δt the time step, $\Delta\omega = 2\pi\Delta f = 2\pi/(N\Delta t)$ the angular frequency step and $t_0 = n_0\Delta t$ the FT starting instant. In Eq. (A.4), Parseval's theorem has been applied. The normalisation ensures that summing the FT PS from DC up to the sampling frequency, yields the signal energy over the investigated time window.

Appendix B. Signal power spectrum with white noise around the Larmor frequency

This Appendix pertains to Section 2.2.1. With white noise $\eta(t)$ around the Larmor frequency, the PS of $u_L(t)$ reads

$$|U_L(\omega, n_0\Delta t, N\Delta t)|^2 = \left(\sqrt{\Delta t/N} \sum_{m=n_0}^{n_0+N-1} [s_L(m\Delta t) + \eta(m\Delta t)] e^{-i\omega m\Delta t}\right)^* \cdot \left(\sqrt{\Delta t/N} \sum_{n=n_0}^{n_0+N-1} [s_L(n\Delta t) + \eta(n\Delta t)] e^{-i\omega n\Delta t}\right) \tag{B.1}$$

$$\overset{s,\eta\in\mathbb{R}}{=} \frac{\Delta t}{N} \sum_{m,n} [s_L(m\Delta t)s_L(n\Delta t) + \eta(m\Delta t)s_L(n\Delta t) + \eta(n\Delta t)s_L(m\Delta t) + \eta(m\Delta t)\eta(n\Delta t)] e^{i\omega m\Delta t} e^{-i\omega n\Delta t} \tag{B.2}$$

$$\overset{\eta\perp se^{(\cdot)}}{\approx} \frac{\Delta t}{N} \sum_{m,n} [s_L(m\Delta t)s_L(n\Delta t) + \eta(m\Delta t)\eta(n\Delta t)] \cdot e^{i\omega m\Delta t} e^{-i\omega n\Delta t} \tag{B.3}$$

$$= \left(\sqrt{\Delta t/N} \sum_m s_L(m\Delta t) e^{-i\omega m\Delta t}\right)^* \cdot \left(\sqrt{\Delta t/N} \sum_n s_L(n\Delta t) e^{-i\omega n\Delta t}\right) + \left(\sqrt{\Delta t/N} \sum_m \eta(m\Delta t) e^{-i\omega m\Delta t}\right)^* \cdot \left(\sqrt{\Delta t/N} \sum_n \eta(n\Delta t) e^{-i\omega n\Delta t}\right) \tag{B.4}$$

$$= |S_L(\omega, n_0\Delta t, N\Delta t)|^2 + |H(\omega, n_0\Delta t, N\Delta t)|^2 \tag{B.5}$$

$$= |S_L(\omega, n_0\Delta t, N\Delta t)|^2 + \sigma_\eta^2, \tag{B.6}$$

where N is the number of samples, Δt the time step, ω the angular frequency and $t_0 = n_0\Delta t$ the FT starting instant. The variance of the noise in the frequency domain is denoted by σ_η^2. In Eq. (B.3), the noise orthogonality (uncorrelatedness) to the signal and the exponential factor is used.

Appendix C. The discrete Fourier transform power spectrum Lorentz peak

This Appendix pertains to Section 2.5.1. Starting from the time-domain FID signal Eq. (1), an analytic form for the discrete FT PS Lorentz peak can be derived. The discrete FT yields for the signal

$$S_L(\omega, 0, N\Delta t) = \sqrt{\frac{\Delta t}{N}} \sum_{n=0}^{N-1} s_L(n\Delta t) e^{-i\omega n\Delta t} \tag{C.1}$$

$$= \sqrt{\frac{\Delta t}{N}} \cdot \frac{A}{2} \sum_{n=0}^{N-1} e^{-n\Delta t/T_2^*} \cdot \left(e^{i\omega_L n\Delta t + i\varphi} + e^{-i\omega_L n\Delta t - i\varphi}\right) e^{-i\omega n\Delta t} \tag{C.2}$$

$$= \sqrt{\frac{\Delta t}{N}} \cdot \frac{A}{2} \left[e^{i\varphi} \frac{e^{-(1/T_2^* - i\omega_L + i\omega)N\Delta t} - 1}{e^{-(1/T_2^* - i\omega_L + i\omega)\Delta t} - 1} + e^{-i\varphi} \frac{e^{-(1/T_2^* + i\omega_L + i\omega)N\Delta t} - 1}{e^{-(1/T_2^* + i\omega_L + i\omega)\Delta t} - 1} \right], \tag{C.3}$$

where N is the number of data points and Δt is the sampling interval. In the second step, Euler's formula was used. The normalisation by $\sqrt{\Delta t/N}$ is described by Eq. (A.4). Now, letting

$$z_\pm = \frac{e^{-(1/T_2^* \pm i\omega_L + i\omega)N\Delta t} - 1}{e^{-(1/T_2^* \pm i\omega_L + i\omega)\Delta t} - 1}, \tag{C.4}$$

Eq. (C.3) may be written as

$$S_L(\omega, 0, N\Delta t) = \sqrt{\frac{\Delta t}{N}} \cdot \frac{A}{2} \left(e^{i\varphi} z_- + e^{-i\varphi} z_+\right). \tag{C.5}$$

The PS follows as

$$|S_L(\omega, 0, N\Delta t)|^2 = \sqrt{\frac{\Delta t}{N}} \cdot \frac{A}{2} \left(e^{i\varphi} z_- + e^{-i\varphi} z_+\right) \cdot \sqrt{\frac{\Delta t}{N}} \left[\frac{A}{2} \left(e^{i\varphi} z_- + e^{-i\varphi} z_+\right)\right]^* \tag{C.6}$$

$$= \frac{\Delta t}{N} \cdot \frac{A^2}{4} \left(z_- z_-^* + z_+ z_+^* + e^{2i\varphi} z_- z_+^* + e^{-2i\varphi} z_+^* z_+\right) \tag{C.7}$$

$$= \frac{\Delta t}{N} \cdot \frac{A^2}{4} \left(z_- z_-^* + z_+ z_+^* + 2\mathrm{Re}\left[e^{2i\varphi} z_- z_+^*\right]\right). \tag{C.8}$$

In the last step, the two last terms are each other's complex conjugates, and only their real parts remain after the summation. The two first terms in Eq. (C.8) can be expanded as

$$z_\pm z_\pm^* = \frac{1 + e^{-2N\Delta t/T_2^*} - 2e^{-N\Delta t/T_2^*} \cos([\omega \pm \omega_L]N\Delta t)}{1 + e^{-2\Delta t/T_2^*} - 2e^{-\Delta t/T_2^*} \cos([\omega \pm \omega_L]\Delta t)}. \tag{C.9}$$

When $N\Delta t/T_2^* \gg 1, 0 \lesssim \Delta t/T_2^* \ll 1$, $[\omega - \omega_L]\Delta t \approx 0$ and $0 < [\omega + \omega_L]\Delta t \approx 2\omega_L\Delta t < \pi$, an approximation for $z_\pm z_\pm^*$ can be obtained:

$$z_\pm z_\pm^* \approx \left[1 + \left(1 - 2\Delta t/T_2^* + 2(\Delta t/T_2^*)^2\right) - 2\left(1 - \Delta t/T_2^* + \frac{1}{2}(\Delta t/T_2^*)^2\right) \times \left(1 - \frac{1}{2}([\omega \pm \omega_L]\Delta t)^2\right)\right]^{-1}, \tag{C.10}$$

where in the numerator, the exponential terms have been approximated to 0, and in the denominator, the exponential functions and the cosine have been approximated up to second order. Expanding, and neglecting the terms with $(\Delta t)^3$ and $(\Delta t)^4$, it follows that

$$z_\pm z_\pm^* \approx \frac{1}{(\Delta t/T_2^*)^2 + [\omega\Delta t \pm \omega_L\Delta t]^2}. \tag{C.11}$$

It can be seen that, when $(1/T_2^*)^2 \ll \omega_L^2$, $z_-z_-^*$ dominates $z_+z_+^*$, so their sum can be approximated as

$$z_-z_-^* + z_+z_+^* \approx z_-z_-^* \tag{C.12}$$

$$\approx \frac{(1/\Delta t)^2}{(1/T_2^*)^2 + (\omega - \omega_L)^2}. \tag{C.13}$$

Now, it remains to show that the last term in Eq. (C.8) can be neglected. The supremum of its absolute value is clearly $|z_-z_+^*|$:

$$|z_-z_+^*| = \sqrt{(z_-z_-^*)(z_+z_+^*)}. \tag{C.14}$$

From Eq. (C.11), it can be seen that Eq. (C.14) is small compared to $z_-z_-^*$. In general, this holds as long as $z_-z_-^*$ is greater than $z_+z_+^*$ by, say, four decades. This makes $|z_-z_+|$ two decades smaller than $z_-z_-^*$ due to the geometric mean in Eq. (C.14). An easy criterion for neglecting the last term in Eq. (C.8) is, again, that $(1/T_2^*)^2 \ll \omega_L^2$.

Finally, it follows that

$$|S_L(\omega, 0, N\Delta t)|^2 \approx \frac{A^2}{4N\Delta t} \cdot \frac{1}{(1/T_2^*)^2 + (\omega - \omega_L)^2}. \tag{C.15}$$

Accordingly, the peak height at ω_L is approximately $(AT_2^*)^2/(4N\Delta t)$ when $\omega_L \gg 1/T_2^*$, $0 \lesssim \Delta t/T_2^* \ll 1$, $(\omega - \omega_L)\Delta t \approx 0$, $0 < (\omega + \omega_L)\Delta t \approx 2\omega_L\Delta t < \pi$ and $N\Delta t/T_2^* \gg 1$.

Starting from Eq. (C.2), it can also be seen that for an exponentially attenuated signal $e^{i\omega_L n\Delta t + i\varphi}$, the PS Lorentzian has the same form as in Eq. (C.15), with the same assumptions as in the case of the real sinusoid given above. The only difference is that the solution is multiplied by $2^2 = 4$. Using Eq. (C.15), it is also easy to prove that the full width at half maximum (FWHM) is $\Delta f_{FWHM} = 1/(\pi T_2^*)$, both in the case of the real and complex FID signal. Eventually, when $\varphi = 0$, the forms of the absorption Lorentzian and the PS Lorentzian are the same up to a constant coefficient [1]. However, as φ starts deviating from *0*, the absorption Lorentzian loses its peak-like form. The same does not happen with the PS Lorentzian, which makes the latter ideal for finding T_2^*, A and f_L, when φ is unknown.

C.1. Slightly approximated power spectrum Lorentz peak shape

This Appendix Subsection pertains to Section 2.2.2. Using Eq. (C.8), the PS Lorentz peak shape can be slightly approximated by

$$|S_L(\omega, 0, N\Delta t)|^2 = \frac{\Delta t}{N} \cdot \frac{A^2}{4}\left(z_-z_-^* + z_+z_+^* + 2\mathrm{Re}\left[e^{2i\varphi} z_-z_+^*\right]\right) \tag{C.16}$$

$$\approx \frac{\Delta t}{N} \cdot \frac{A^2}{4} z_-z_-^* \tag{C.17}$$

$$= \frac{\Delta t}{N} \cdot \frac{A^2}{4} \cdot \frac{1 + e^{-2N\Delta t/T_2^*} - 2e^{-N\Delta t/T_2^*}\cos([\omega - \omega_L]N\Delta t)}{1 + e^{-2\Delta t/T_2^*} - 2e^{-\Delta t/T_2^*}\cos([\omega - \omega_L]\Delta t)}, \tag{C.18}$$

where N is the number of samples in the time-domain signal. The approximation above is justified as long as $\omega_L^2 \gg (1/T_2^*)^2$.

Appendix D. Noise considerations in the integral exponential fit vector products

This Appendix pertains to Section 2.3, where the variable definitions can be found. Thus, the noise of the vector products in the solutions of $\hat{b}$ and $\hat{c}$ can be considered:

$$|\mathbf{x}|^2 = |\mathbf{x}_0 + \boldsymbol{\mu}|^2 \tag{D.1}$$

$$= |\mathbf{x}_0|^2 + |\boldsymbol{\mu}|^2 + 2\mathbf{x}_0^T\boldsymbol{\mu} \tag{D.2}$$

$$\overset{\mathbf{x}_0 \perp \boldsymbol{\mu}}{\approx} |\mathbf{x}_0|^2 + \sum_{k=1}^{M}(\mu_{n_k} - \mu_{m_k})^2 + 0 \tag{D.3}$$

$$\overset{\text{only } \mu_m\mu_n \sim \delta_{m,n}\sigma_\mu^2}{\approx} |\mathbf{x}_0|^2 + 2M\sigma_\mu^2, \tag{D.4}$$

$$|\mathbf{y}|^2 \approx |\mathbf{y}_0|^2 + 2M\sigma_\nu^2, \tag{D.5}$$

$$\mathbf{x}^T\mathbf{y} = (\mathbf{x}_0 + \boldsymbol{\mu})^T(\mathbf{y}_0 + \boldsymbol{\nu}) \tag{D.6}$$

$$= \mathbf{x}_0^T\mathbf{y}_0 + \mathbf{x}_0^T\boldsymbol{\nu} + \mathbf{y}_0^T\boldsymbol{\mu} + \boldsymbol{\mu}^T\boldsymbol{\nu} \tag{D.7}$$

$$\overset{\mathbf{x}_0 \perp \boldsymbol{\nu}, \mathbf{y}_0 \perp \boldsymbol{\mu}, \boldsymbol{\mu} \perp \boldsymbol{\nu}}{\approx} \mathbf{x}_0^T\mathbf{y}_0, \tag{D.8}$$

$$\mathbf{y}^T\mathbf{Y} = \sum_{k=1}^{M}(y_{n_k} - y_{m_k})\sum_{n=m_k}^{n_k-1}(x_{n+1} - x_n)\frac{y_n + y_{n+1}}{2} \tag{D.9}$$

$$= \sum_{k=1}^{M}(y_{n_k} - y_{m_k})\left[(x_{m_k+1} - x_{m_k})\frac{y_{m_k} + y_{m_k+1}}{2} + (x_{n_k} - x_{n_k-1})\frac{y_{n_k-1} + y_{n_k}}{2} + \sum_{n=m_k+1}^{n_k-2}(x_{n+1} - x_n)\frac{y_n + y_{n+1}}{2}\right] \tag{D.10}$$

$$\overset{\text{only } \nu_m\nu_n \sim \delta_{m,n}\sigma_\nu^2}{\approx} \sum_{k=1}^{M}\left\{(y_{0,n_k} - y_{0,m_k})\left[(x_{0,m_k+1} - x_{0,m_k})\frac{y_{0,m_k} + y_{0,m_k+1}}{2} + (x_{0,n_k} - x_{0,n_k-1})\frac{y_{0,n_k-1} + y_{0,n_k}}{2} + \sum_{n=m_k+1}^{n_k-2}(x_{0,n+1} - x_{0,n})\frac{y_{0,n} + y_{0,n+1}}{2}\right] + (x_{n_k+1} - x_{n_k})\nu_{n_k}^2/2 - (x_{m_k+1} - x_{m_k})\nu_{m_k}^2/2\right\} \tag{D.11}$$

$$\approx \sum_{k=1}^{M}\left\{(y_{0,n_k} - y_{0,m_k})\sum_{n=m_k}^{n_k-1}(x_{0,n+1} - x_{0,n})\frac{y_{0,n} + y_{0,n+1}}{2} + (x_{n_k} - x_{n_k-1})\sigma_\nu^2/2 - (x_{m_k+1} - x_{m_k})\sigma_\nu^2/2\right\} \tag{D.12}$$

$$\overset{x_{m_k+1} - x_{m_k} \approx x_{n_k} - x_{n_k-1}}{\approx} \mathbf{y}_0^T\mathbf{Y}_0 \quad \text{and} \tag{D.13}$$

$$\mathbf{x}^T\mathbf{Y} = \sum_{k=1}^{M}(x_{n_k} - x_{m_k})\sum_{n=m_k}^{n_k-1}(x_{n+1} - x_n)\frac{y_n + y_{n+1}}{2} \tag{D.14}$$

$$= \sum_{k=1}^{M}(x_{n_k} - x_{m_k})\left[(x_{m_k+1} - x_{m_k})\frac{y_{m_k} + y_{m_k+1}}{2} + (x_{n_k} - x_{n_k-1})\frac{y_{n_k-1} + y_{n_k}}{2} + \sum_{n=m_k+1}^{n_k-2}(x_{n+1} - x_n)\frac{y_n + y_{n+1}}{2}\right] \tag{D.15}$$

$$\overset{\text{only } \mu_m\mu_n \sim \delta_{m,n}\sigma_\mu^2}{\approx} \sum_{k=1}^{M}\left\{(x_{0,n_k} - x_{0,m_k})\left[(x_{0,m_k+1} - x_{0,m_k})\frac{y_{0,m_k} + y_{0,m_k+1}}{2} + (x_{0,n_k} - x_{0,n_k-1})\frac{y_{0,n_k-1} + y_{0,n_k}}{2} + \sum_{n=m_k+1}^{n_k-2}(x_{0,n+1} - x_{0,n})\frac{y_{0,n} + y_{0,n+1}}{2}\right] + \mu_{m_k}^2\frac{y_{m_k} + y_{m_k+1}}{2} + \mu_{n_k}^2\frac{y_{n_k-1} + y_{n_k}}{2}\right\} \tag{D.16}$$

$$\overset{y_{m_k} \approx y_{m_k+1}, y_{n_k-1} \approx y_{n_k}}{\approx} \mathbf{x}_0^T\mathbf{Y}_0 + \sum_{k=1}^{M}\sigma_\mu^2(y_{m_k} + y_{n_k}) \tag{D.17}$$

$$= \mathbf{x}_0^T\mathbf{Y}_0 + \sigma_\mu^2(\mathbf{y}^+)^T\mathbf{1}, \tag{D.18}$$

where the elements of the vector $\mathbf{y}_0^+$ are sums of the noiseless y coordinates at the integration limits $\left(y_k^+ = y_{m_k} + y_{n_k}\right)$. In the

approximations, where two vectors are denoted perpendicular, uncorrelatedness is used. The approximations containing the word 'only' assume that only the terms with a square of noise remain from the terms containing noise. The approximations showing a perpendicularity ($\perp$) sign indicate that the inner product of the vectors beside the sign averages to approximately 0.

Appendix E. Using iteration to obtain the optimal integral exponential fit

This Appendix pertains to Section 2.3. If the noise level of the data points is known, this step is not needed, and the integral fitting algorithm is completely non-iterative. However, the noise level can also be evaluated over a few iterative fits. Here, it is assumed that the x direction is free of noise, but the noise in the y direction is present. The following method works as long as the calculated fit error forms a convex curve with respect to the noise level estimate in the performed exponential fit. This was experimentally found to be the case.

There are two noise levels to consider first: $\sigma_{v,\min} = 0$ and $\sigma_{v,\max}$. The former one represents no noise at all in the data points' fit. The latter one represents the maximum possible noise level after fitting a straight line to the data points. The line has no plasticity to adapt to the data points so, in this treatment, it gives the worst-case noise for the optimised exponential fit.

The iteration is based on choosing five equispaced values for the noise levels, starting from the minimum noise level and ending in the maximum one. Then, the fit is performed with all of these noise levels, and the corresponding fit errors are computed. The minimum error is located, whereafter the minimum and maximum noise levels are updated to be around the minimum fit error. Again, new fit errors are computed at five equispaced points in the span of the updated minimum and maximum noise levels. The detailed algorithm is presented below.

E.1. Definitions

1. There are altogether P elements in the data vectors $\mathbf{x}$ and $\mathbf{y}$.
2. The exponential fit by integration:
   - Parameter estimates at noise level σ_v: $\hat{a}(\sigma_v), \hat{b}(\sigma_v), \hat{c}(\sigma_v)$
   - Fit: $[\mathbf{y}_e(\sigma_v)]_k = \hat{a}(\sigma_v)e^{\hat{b}(\sigma_v)[\mathbf{x}]_k} + \hat{c}(\sigma_v)$
3. The LS fit of a line:
   - Parameter estimates: $\hat{\alpha}, \hat{\beta}$
   - Fit: $\mathbf{y}_l = \hat{\alpha}\mathbf{x} + \hat{\beta}$

Algorithm.

1. Initialise a minimum and maximum noise level:
   - $\sigma_{v,\min}[0] = 0$
   - $\sigma_{v,\max}[0] = \sqrt{\frac{1}{P}|\mathbf{y}_l - \mathbf{y}|^2}$
   - $n = 0$
2. Compute the noise level interval:
   - $\Delta\sigma_v[n] = \sigma_{v,\max}[n] - \sigma_{v,\min}[n]$
3. Compute five fit errors:
   - $\varepsilon[n,m] = \sqrt{\frac{1}{P}|\mathbf{y}_e(\sigma_{v[n],\min}[n] + \frac{m}{4}\cdot\Delta\sigma_v[n]) - \mathbf{y}|^2}, \quad m \in \{0,1,2,3,4\}$
4. Update the noise levels:
   - $k = \underset{m\in\{0,1,2,3,4\}}{\arg\min}\ \varepsilon[n,m]$
   - If $k = 0$, set $k = 1$; if $k = 4$, set $k = 3$.
   - $\sigma_{v,\min}[n+1] = \sigma_{v,\min}[n] + \frac{k-1}{4}\cdot\Delta\sigma_v[n]$
   - $\sigma_{v,\max}[n+1] = \sigma_{v,\min}[n] + \frac{k+1}{4}\cdot\Delta\sigma_v[n]$
   - $n = n + 1$
5. Repeat from step 2 until the desired level of convergence is achieved.
6. The resulting noise level estimate is
   - $\sigma_v = \frac{\sigma_{v,\min}[n]+\sigma_{v,\max}[n]}{2}$

This algorithm reduces the search interval for the optimum noise level by 50% at each step of the iteration. In the end, the noise level and fit error do not generally completely agree. In other words, the noise level can be used as a kind of parameter which can be adjusted to get the fit with least error through the scattered data points.

Appendix F. Noise considerations for the Lorentz peak shape fitting

This Appendix pertains to Section 2.4. Starting from the FID signal's noise η that is white around the Larmor frequency, with standard deviation σ_η, the effect of noise in the LS solution of Eq. (36) can be studied.

F.1. The noise power spectrum and its square

The PS of the FID signal's noise is

$$|H(\omega,0,N\Delta t)|^2 = \frac{\Delta t}{N}\left|\sum_{m=0}^{N-1}\eta(m)e^{-i\omega m\Delta t}\right|^2 \tag{F.1}$$

$$= \frac{\Delta t}{N}\sum_{m,n}\eta(m)\eta(n)e^{-i\omega(m-n)\Delta t} \tag{F.2}$$

$$\approx \sigma_\eta^2. \tag{F.3}$$

The square of the noise PS is of the order σ_η^4, where σ_η is small, so the approximation

$$|H(\omega,0,N\Delta t)|^4 \approx 0 \tag{F.4}$$

is made.

F.2. The Larmor signal power spectrum and its square with noise

Now, after knowing these noise power-spectral properties, the measured PSs can be better evaluated, starting from the time-domain signal

$$|y|^2 = \frac{\Delta t}{N}\left|\sum_{m=0}^{N-1}(s_L(m) + \eta(m))e^{-i\omega m\Delta t}\right|^2 \tag{F.5}$$

$$\approx |y_{01}|^2 + |H(\omega,0,N\Delta t)|^2 \tag{F.6}$$

$$\approx |y_{01}|^2 + \sigma_\eta^2, \tag{F.7}$$

where $|y_{01}|^2$ is the noiseless signal, and Eq. (F.3) has been used.

The same kind of analysis has to be carried out for $|y|^4$, marking the corrected variable with $|y_{02}|^4$:

$$|y|^4 = \left(\frac{\Delta t}{N}\right)^2\left|\sum_{m=0}^{N-1}[s_L(m) + \eta(m)]e^{-i\omega m\Delta t}\right|^4 \tag{F.8}$$

$$= \left(\frac{\Delta t}{N}\right)^2\sum_{k,l,m,n}[s_L(k) + \eta(k)][s_L(l) + \eta(l)][s_L(m) + \eta(m)] \cdot [s_L(n) + \eta(n)]e^{-i\omega(k-l+m-n)\Delta t} \tag{F.9}$$

$$\approx |y_{02}|^4 + 4|y_{01}|^2\sigma_\eta^2, \tag{F.10}$$

where in the last step, Eqs. (F.3) and (F.4) have been applied, neglecting all terms with σ_η^4.

Appendix G. Derivation of the functional form of the correlation curve

This Appendix pertains to Section 2.5.2. The correlation is evaluated by

$$c\{s_L(\tilde{\varphi},n\Delta t),u_L(\varphi,n\Delta t)\}=\sum_{n=0}^{N-1}\tilde{s}_L(\tilde{\varphi},n\Delta t)u_L(\varphi,n\Delta t) \tag{G.1}$$

$$=\sum_n\left[A^2e^{-2n\Delta t/T_2^*}\cos(\omega_L n\Delta t+\tilde{\varphi})\cos(\omega_L n\Delta t+\varphi)\right.$$
$$\left.+Ae^{-n\Delta t/T_2^*}\cos(\omega_L n\Delta t+\tilde{\varphi})\eta(n\Delta t)\right] \tag{G.2}$$

$$\overset{\eta\perp e^{(\cdot)}\cos(\cdot)}{\approx}\sum_n A^2e^{-2n\Delta t/T_2^*}\frac{1}{4}\left[e^{i(\omega_L n\Delta t+\tilde{\varphi})}+e^{-i(\omega_L n\Delta t+\tilde{\varphi})}\right]$$
$$\cdot\left[e^{i(\omega_L n\Delta t+\varphi)}+e^{-i(\omega_L n\Delta t+\varphi)}\right] \tag{G.3}$$

$$=\frac{1}{4}A^2\sum_n\left[e^{-2n\Delta t/T_2^*+i(2\omega_L n\Delta t+\tilde{\varphi}+\varphi)}\right.$$
$$+e^{-2n\Delta t/T_2^*-i(2\omega_L n\Delta t+\tilde{\varphi}+\varphi)}$$
$$\left.+e^{-2n\Delta t/T_2^*+i(\tilde{\varphi}-\varphi)}+e^{-2n\Delta t/T_2^*-i(\tilde{\varphi}-\varphi)}\right] \tag{G.4}$$

$$=\frac{1}{4}A^2\left[\frac{e^{i(\tilde{\varphi}+\varphi)}\left(1-e^{-2N\Delta t/T_2^*+2Ni\omega_L\Delta t}\right)}{1-e^{-2\Delta t/T_2^*+2i\omega_L\Delta t}}\right.$$
$$+\frac{e^{-i(\tilde{\varphi}+\varphi)}\left(1-e^{-2N\Delta t/T_2^*-2Ni\omega_L\Delta t}\right)}{1-e^{-2\Delta t/T_2^*-2i\omega_L\Delta t}}$$
$$\left.+\frac{1-e^{-2N\Delta t/T_2^*}}{1-e^{-2\Delta t/T_2^*}}\left(e^{i(\tilde{\varphi}-\varphi)}+e^{-i(\tilde{\varphi}-\varphi)}\right)\right] \tag{G.5}$$

$$=\frac{1}{4}A^2\left[\left\{e^{i(\tilde{\varphi}+\varphi)}\left(1-e^{-2N\Delta t/T_2^*+2Ni\omega_L\Delta t}\right)\right.\right.$$
$$\cdot\left(1-e^{-2\Delta t/T_2^*-2i\omega_L\Delta t}\right)$$
$$\left.\left.+e^{-i(\tilde{\varphi}+\varphi)}\left(1-e^{-2N\Delta t/T_2^*-2Ni\omega_L\Delta t}\right)\left(1-e^{-2\Delta t/T_2^*+2i\omega_L\Delta t}\right)\right\}\right.$$
$$\div\left(1-2e^{-2\Delta t/T_2^*}\cos(2\omega_L\Delta t)+e^{-4\Delta t/T_2^*}\right)$$
$$\left.+2\frac{1-e^{-2N\Delta t/T_2^*}}{1-e^{-2\Delta t/T_2^*}}\cos(\tilde{\varphi}-\varphi)\right] \tag{G.6}$$

$$\overset{\Delta t/T_2^*\ll1}{\approx}\frac{1}{4}A^2[\{2\cos(\tilde{\varphi}+\varphi)$$
$$-2e^{-2N\Delta t/T_2^*}\cos(2N\omega_L\Delta t+\tilde{\varphi}+\varphi)$$
$$-2e^{-2\Delta t/T_2^*}\cos(-2\omega_L\Delta t+\tilde{\varphi}+\varphi)$$
$$+2e^{-2(N+1)\Delta t/T_2^*}\cos(2(N-1)\omega_L\Delta t+\tilde{\varphi}+\varphi)\}$$
$$\div\left(1-2(1-2\Delta t/T_2^*+2\left[\Delta t/T_2^*\right]^2)(1-2[\omega_L\Delta t]^2)\right.$$
$$\left.+\left(1-4\Delta t/T_2^*+8[\Delta t/T_2^*]^2\right)\right)$$
$$\left.+2\frac{1-e^{-2N\Delta t/T_2^*}}{1-(1-2\Delta t/T_2^*)}\cos(\tilde{\varphi}-\varphi)\right] \tag{G.7}$$

$$\overset{\Delta t/T_2^*\ll1,\omega_L\Delta t<1}{\approx}\frac{1}{4}A^2[\{\cos(\tilde{\varphi}+\varphi)$$
$$-e^{-2N\Delta t/T_2^*}\cos(2N\omega_L\Delta t+\tilde{\varphi}+\varphi)$$
$$-e^{-2\Delta t/T_2^*}\cos(-2\omega_L\Delta t+\tilde{\varphi}+\varphi)$$
$$+e^{-2(N+1)\Delta t/T_2^*}\cos(2(N-1)\omega_L\Delta t+\tilde{\varphi}+\varphi)\}$$
$$\div\left(2\left[\Delta t/T_2^*\right]^2+2[\omega_L\Delta t]^2\right)$$
$$\left.+\frac{1-e^{-2N\Delta t/T_2^*}}{\Delta t/T_2^*}\cos(\tilde{\varphi}-\varphi)\right] \tag{G.8}$$

$$\approx\frac{1}{4}A^2\left[\frac{1+e^{-2N\Delta t/T_2^*}}{(\Delta t/T_2^*)^2+(\omega_L\Delta t)^2}\right.$$
$$\left.+\frac{1-e^{-2N\Delta t/T_2^*}}{\Delta t/T_2^*}\cos(\tilde{\varphi}-\varphi)\right] \tag{G.9}$$

$$\overset{(\omega_L\Delta t)^2\gg\Delta t/T_2^*}{\approx}\frac{1}{4}A^2\frac{1-e^{-2N\Delta t/T_2^*}}{\Delta t/T_2^*}\cos(\tilde{\varphi}-\varphi) \tag{G.10}$$

$$\propto\cos(\tilde{\varphi}-\varphi). \tag{G.11}$$

In step (G.3), it is assumed that the measured FID's noise is uncorrelated with the modelled FID. In step (G.7), $\Delta t/T_2^*$ is assumed small. In the following step, in addition, $\omega_L\Delta t$ is less than 1. In step (G.9), the first of the two quotients in the previous step is approximated by a maximum limit, so in the next step it can be seen that only the last quotient will remain significant when $(\omega_L\Delta t)^2\gg\Delta t/T_2^*$. The final result shows that the correlation is directly proportional to a cosine as long as the temporal length of the correlation is constant and the other approximations hold.

References

[1] M.H. Levitt, Spin Dynamics — Basics of Nuclear Magnetic Resonance, John Wiley & Sons, Ltd., Chichester, England, 2006.
[2] H. Günther, NMR Spectroscopy: Basic Principles, Concepts, and Applications in Chemistry, John Wiley & Sons, Chichester, England, 2001.
[3] A.G. Marshall, F.R. Verdun, Fourier Transforms in NMR, Optical, and Mass Spectrometry, Elsevier, Amsterdam, the Netherlands, 1990.
[4] I. Kitagawa, Relaxation time specifying and spectrum assignment determining method and measuring result display method, Technical report, Hitachi Ltd., European Patent Office JP2006317311, November 2006.
[5] H. Barkhuijsen, R. de Beer, D. van Ormondt, Improved algorithm for noniterative time-domain model fitting to exponentially damped magnetic resonance signals, J. Magn. Reson. 73 (1987) 553–557.
[6] G.L. Millhauser, A.A. Carter, D.J. Schneider, J.H. Freed, R.E. Oswald, Rapid singular value decomposition for time-domain analysis of magnetic resonance signals by use of the Lanczos algorithm, J. Magn. Reson. 82 (1989) 150–155.
[7] T. Laudadio, N. Mastronardi, L. Vanhamme, P. van Hecke, S. van Huffel, Improved Lanczos algorithms for blackbox MRS data quantitation, J. Magn. Reson. 157 (2002) 292–297.
[8] N. Mastronardi, M. Schuermans, M. van Barel, R. Vandebril, S. van Huffel, The Lanczos reduction to semiseparable matrices, Katholieke Universiteit Leuven, 2005 (<ftp://ftp.esat.kuleuven.ac.be/pub/SISTA/ida/reports/05-63.pdf>, viewed in April 2010).
[9] P. Mutzenhardt, J. Brondeau, F. Humbert, D. Canet, Algorithm based on a new proof of HSVD equations derived without invoking singular-value decomposition, J. Magn. Reson. 94 (1991) 543–549.
[10] H. Chen, S. van Huffel, C. Decanniere, P. van Hecke, A signal-enhancement algorithm for the quantification of NMR data in the time domain, J. Magn. Reson. A 109 (1994) 46–55.
[11] H. Chen, S. van Huffel, R. van Ormondt, D. de Beer, Parameter estimation with prior knowledge of known signal poles for the quantification of NMR spectroscopy data in the time domain, J. Magn. Reson. A 119 (1996) 225–234.
[12] P. Koehl, Linear prediction spectral analysis of NMR data, Prog. Nucl. Magn. Reson. Spectrosc. 34 (1999) 257–299.
[13] S.B. Engelsen, R. Bro, PowerSlicing, J. Magn. Reson. 163 (2003) 192–197.
[14] T. Laudadio, Subspace-based quantification of magnetic resonance spectroscopy data using biochemical prior knowledge, Ph.D. thesis, Katholieke Universiteit Leuven, December 2005.
[15] R. de Beer, c59 quantitative in vivo NMR, Lecture notes of a course, Department of Applied Physics, University of Technology Delft, 1994–2003.
[16] L. Vanhamme, T. Sundin, P. van Hecke, S. van Huffel, MR spectroscopy quantitation: a review of time-domain methods, NMR Biomed. 14 (2001) 233–246.
[17] M. Ohuchi, S. Uchida, Phase correction method in two-dimensional NMR spectroscopy, Technical report, Jeol Ltd., United States Patent US4766377, August 1988.
[18] I. Miura, M. Miyake, Solid sample nuclear magnetic resonance measuring method, Technical report, Otsuka Pharmaceutical Co., Ltd., European Patent Application EP1772741, April 2007.
[19] J.J. van Vaals, Method of and device for automatic phase correction of complex NMR spectra, Technical report, Philips NV, European Patent Application EP0316041, May 1989.
[20] R. Dunkel, Method for correcting spectral and imaging data and for using such corrected data in magnet shimming, Technical report, United States Patent US5218299, June 1993.
[21] D.S. Wishart, R. Greiner, T.A. Rosborough, B.A. Lefebvre, N.A. Epstein, J.B. Newton, W.R. Wong, Automatic identification of compounds in a sample mixture by means of NMR spectroscopy, Technical report, United States Patent US20040058386, March 2004.
[22] S.D. Foss, A method of exponential curve fitting by numerical integration, Biometrics 26 (4) (1970) 815–821.
[23] D. Halmer, G. von Basum, P. Hering, M. Mürtz, Fast exponential fitting algorithm for real-time instrumental use, Rev. Sci. Instrum. 75 (6) (2004) 2187–2191.
[24] The MathWorks, MATLAB Curve Fitting Toolbox™ 1 — User's Guide, 2010 (<http://www.mathworks.com/access/helpdesk/help/pdf_doc/curvefit/curvefit.pdf>, viewed in April 2010).
[25] Z. Jeričević, Method for fitting a sum of exponentials to experimental data by linearization using a numerical integration approximation, and its application to well log data, Technical report, KJT Enterprises, Inc., Houston, TX, United States Patent US007088097B2, August 2006.
[26] J.-B. Poullet, D.M. Sima, S. van Huffel, MRS signal quantitation: a review of time- and frequency-domain methods, J. Magn. Reson. 195 (2008) 134–144.
[27] L. Qiu, Y. Zhang, H.-J. Krause, A.I. Braginski, M. Burghoff, L. Trahms, Nuclear magnetic resonance in the earth's magnetic field using a nitrogen-cooled superconducting quantum interference device, Appl. Phys. Lett. 91 (2007) 072505.
[28] H. Dong, Y. Wang, S. Zhang, Y. Sun, X. Xie, Detection of proton NMR signal in the Earth's magnetic field at an urban laboratory environment without shielding, Supercond. Sci. Technol. 21 (2008) 115009.
[29] R. Koskinen, M. Lehto, H. Väänänen, J. Rantonen, L.-M. Voipio-Pulkki, M. Mäkijärvi, L. Lehtonen, J. Montonen, L. Toivonen, Measurement and reproducibility of magnetocardiographic filtered atrial signal in patients with paroxysmal lone atrial fibrillation and in healthy subjects, J. Electrocardiol. 38 (2005) 330–336.

[30] W. Myers, D. Slichter, M. Hatridge, S. Busch, M. Mößle, R. McDermott, A. Trabesinger, J. Clarke, Calculated signal-to-noise ratio of MRI detected with SQUIDs and Faraday detectors in fields from 10 μt to 1.5 T, J. Magn. Reson. 186 (2007) 182–192.
[31] R. McDermott, A.H. Trabesinger, M. Mück, E.L. Hahn, A. Pines, J. Clarke, Liquid-state NMR and scalar couplings in microtesla magnetic fields, Science 295 (2002) 2247–2249.
[32] M. Burghoff, S. Hartwig, L. Trahms, Nuclear magnetic resonance in the nanotesla range, Appl. Phys. Lett. 87 (2005) 054103.
[33] Y. Zhang, L. Qiu, H.-J. Krause, Liquid state nuclear magnetic resonance at low fields using a nitrogen cooled superconducting quantum interference device, Appl. Phys. Lett. 90 (2007) 182503.